

# Performance of the FIRST, a Longwave Infrared Hyperspectral Imaging Sensor

Vincent Farley<sup>\*a</sup>, Alexandre Vallières<sup>a</sup>, Martin Chamberland<sup>a</sup>, André Villemaire<sup>a</sup>,  
and Jean-François Legault<sup>b</sup>

<sup>a</sup>Telops inc., 100-2600 St-Jean-Baptiste, Québec, Qc, Canada G2E 6J5

<sup>b</sup>Telops USA inc., 3201 Stellhorn Road, Fort Wayne, Indiana 46815, USA

## ABSTRACT

Emerging applications in Defense and Security require sensors with state-of-the-art sensitivity and capabilities. Among these sensors, the imaging spectrometer is an instrument yielding a large amount of rich information about the measured scene. Standoff detection, identification and quantification of chemicals in the gaseous state are fundamental needs in several fields of applications. Imaging spectrometers have unmatched capabilities to meet the requirements of these applications.

Telops has developed the FIRST, a LWIR hyperspectral imager. The FIRST is based on FTIR technology to provide high spectral resolution and to enable high accuracy radiometric calibration. The FIRST, a man portable sensor, provides datacubes of up to 320x256 pixels at 0.35 mrad spatial resolution over the 8-12  $\mu\text{m}$  spectral range at spectral resolutions of up to 0.25  $\text{cm}^{-1}$ . The FIRST has been used in several field measurements, including demonstration of standoff chemical agent detection. One key feature of the FIRST is its ability to give calibrated measurements. The quality of the calibrated measurements will be presented in this paper.

Sensitivity, spectral resolution and radiometric stability as obtained during field and laboratory measurements will be presented. Finally, images of chemical releases detected with the FIRST will be shown.

Keywords: hyperspectral imaging, imaging spectrometry, imaging FTS, FTIR, standoff detection, remote sensing, radiometric calibration, thermal infrared

## 1. Introduction

Chemical warfare is becoming a growing concern in modern military operations. Chemical agents and Toxic Industrial Chemicals (TICs) are indeed insidious weapons since they are generally colourless and odourless which makes them very difficult to detect by conventional means. Chemical attacks are particularly devastating on loss of life and troop moral. It is thus a most invaluable tool to be able to detect and to predict the evolution of contaminant clouds as they explode from munitions or are released by other means.

The most effective chemical standoff sensors against such attacks are based on passive infrared spectroradiometers. In recent years, high-performance and relatively low cost IR imaging (multi-element) detectors have become available. This has made possible the development of a new breed of passive infrared spectroradiometers; imaging sensors such as Telops' FIRST. This sensor is the fusion of two field-proven technologies: the passive infrared spectroradiometers and the infrared camera. In this paper, we present laboratory and field tests results obtained with the FIRST that expose the outstanding performances of this innovative commercial of-the-shelf instrument.

The FIRST sensor is described in section 2. Sections 3 and 4 respectively present the spatial and spectral resolution of the FIRST. In section 5, the sensitivity of the sensor is described in terms of NESR. The accuracy and stability of the radiometric data acquired, two primordial characteristics reported in section 6, prove the unmatched performance of the FIRST. Finally, the unparalleled capabilities of the FIRST for standoff chemical detection are exposed in section 7.

---

\* vincent.farley@telops.com; phone (418) 864-7808; fax (418) 864-7843; www.telops.com

## 2. Description of the FIRST-LW Sensor

The FIRST sensor is a lightweight and compact imaging spectroradiometer. The spectral measurements are performed using a Fourier-Transform Spectrometer (FTS). It uses a 320x256 LWIR PV-MCT focal plane array detector that can be windowed and formatted to fit the desired size and to decrease the acquisition time. Spectral resolution is user-selectable from 0.25 to 150  $\text{cm}^{-1}$ . This instrument measures the complete spectrum of each pixel in the image, each pixel having an instantaneous field-of-view of 0.35 mrad. The latest version of this field-portable sensor is shown in Figure 1. This version is conduction-cooled and sealed from the environment. It is thus ideally designed to withstand operation in harsh and dusty conditions.



Figure 1: Photograph of the FIRST sensor

The instrument features 2 internal calibration blackbodies used to perform a complete end-to-end radiometric calibration of the measurements (see Section 4). In its longwave IR version, the instrument has good sensitivity over the 8-12  $\mu\text{m}$  band. This spectral band is ideal for standoff chemical agent detection at ambient temperatures. The sensor also has acquisition and processing electronics, including 4 GB of high-speed DDR-SDRAM, with the capability to convert the raw interferograms into spectra using real-time Discrete-Fourier Transform (DFT).

The instrument outputs the measurements on a high-speed CameraLink interface. The configuration, monitoring and real-time housekeeping data collection is performed using an Ethernet link. A bore-sight video camera takes simultaneous visible images aligned with the imaging FTS. The instrument supports two operating modes: FTS mode and Camera mode. In Camera mode, the instrument generates a standard broadband thermal IR digital video and supports up to 300 frames per second with the full 320 x 256 pixels of the focal plane array area. In FTS mode, the interferograms or the spectra are transferred along with a header containing all configuration parameters and monitored values to be stored on the computer.

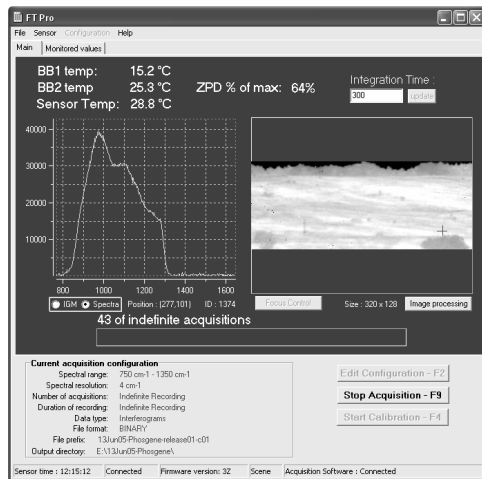


Figure 2: FTPro™ control software

The FTPro™ control software provides a user-friendly interface, giving real-time feedback to the operator. A screenshot of the control software is presented in Figure 2 on the left-hand side. On the right panel, the non-uniformity corrected broadband IR image is displayed in grayscale where black corresponds to low radiance level and white corresponds to high radiance level. The uncalibrated raw spectrum (or the interferogram as selected by the operator) of a selected pixel in the image is displayed in real time on the left of the screen. Additional key parameters such as the blackbodies temperature, the sensor temperature and the level of signal on the FPA are also displayed. Additional monitored values can be viewed in a separate panel. This main panel of the user interface is used to start the acquisition of the data or to initiate calibration measurements. The configuration of the sensor (image size and location, spectral resolution, blackbody and sensor temperatures, etc...) is performed with another input panel. The integration time of the FPA can be changed from the main panel.

The sensor has the capability to change the focus of the IR image to produce a clear image at any distance from 2 meters up to infinity. The FIRST was presented in detail in previous papers [4, 5, 6 and 7].

### 3. Spatial Resolution

To produce a high-quality IR image of the scene, Telops designed the optical assembly such that the blur is smaller than the diffraction from this  $f/2$  system. With the FPA's  $30\ \mu\text{m}$  pixels and the lens focal length of 86 mm, a 0.35 mrad IFOV is obtained. The lens produces a pupil image in the interferometer (close to the corner cube) in order to minimize vignetting and maintain high sensitivity without increasing the size of the interferometer. To maintain the high image quality notwithstanding temperature variations, Telops implemented a servo-controlled autofocus. This efficient system allows maintaining the diffraction limited performance over a wide range of temperatures. Figure 3 presents a picture of the lens assembly.

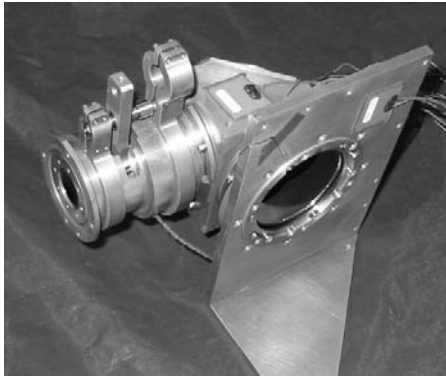


Figure 3: IR lens photograph

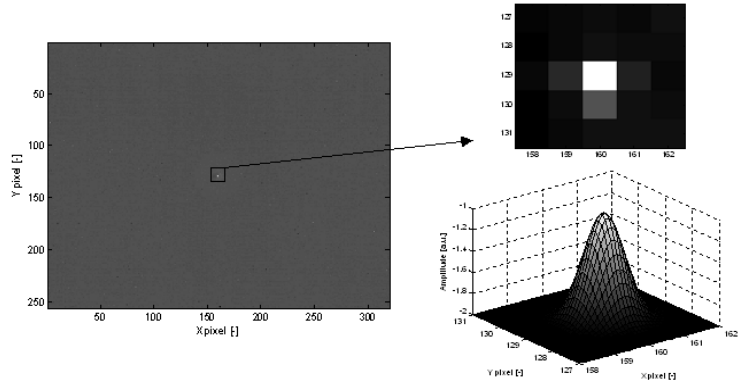


Figure 4: Measured optical blur for a collimated source in the center of the FOV

The optical blur of the system was measured by looking at a collimated hot source. The divergence of the hot source was  $78\ \mu\text{rad}$ , i.e. less than  $\frac{1}{4}$  of a detector pixel. Figure 4 shows the blur spot at the center of the FOV.

Table 1 gives the measured optical blur for different locations in the field-of-view. The optical blur FWHM is of the same order of magnitude as the pixel IFOV ( $350\ \mu\text{rad}$ ), and the autofocus allows achieving this performance for a wide range of temperatures exceeding 0 to  $50^\circ\text{C}$ .

TABLE 1 : Optical blur measurements

POSITION IN FOV	BLUR FWHM [ $\mu\text{rad}$ ]
CENTER	386
TOP-LEFT CORNER	386
TOP-RIGHT CORNER	486
BOTTOM-LEFT CORNER	426
BOTTOM-RIGHT CORNER	419

### 4. Spectral Resolution

Spectral resolution represents the capacity of a sensor to resolve two adjacent frequencies. This parameter is thus one of the most important characteristic of any spectrometer especially for applications that require a narrow spectral resolution and a good spectral accuracy. In this section, the spectral resolution of the FIRST is described.

#### 4.1. Spectral Resolution Concept

An “ideal” FTS could theoretically resolve two frequencies infinitely near to one another. A “real” instrument though, is unable to perform as well because the processing of discrete signals is done on finite length sequences. The truncation limit of the signals is conventionally referred to as *observation window* or simply *window*.

In FTS theory, spectral resolution is usually expressed in one of two ways. It can be defined as the full width at half maximum (FWHM) of the main spectral peak or as the separation between the first zeros of the cardinal sine function

describing the instrument response to an impulse when the data is windowed. Telops uses the FWHM definition to describe the performance of its sensors. Under this assumption, the spectral resolution is evaluated with equation (1):

$$\Delta\sigma_{\text{FWHM}} = 1.2 / 2 \cdot \text{MPD} \tag{1}$$

where  $\Delta\sigma_{\text{FWHM}}$  is the FWHM spectral resolution; [ $\text{cm}^{-1}$ ]  
 MPD is the Maximal Path Difference of the interferometer; [cm].

The Telops interferometer can generate OPDs from  $-0.6$  cm to  $+2.5$  cm. This thus theoretically allows measuring IR spectra with a resolution of  $1 \text{ cm}^{-1}$  in a double-sided mode, and down to  $0.24 \text{ cm}^{-1}$  in a single-sided mode.

#### 4.2. Spectral Resolution: Experimental Results

To test the spectral response of a spectrometer, a spectral impulse is measured by the sensor and the line broadening is analyzed. In order to do so, an adequate spectral target needs to be identified. The target must exhibit at least one very narrow and strong spectral line. Of course, the position of the spectral line must also be accurately known. Water vapor possesses spectral features in the LWIR region of the electromagnetic spectrum, within the spectral range of the FIRST-LW. On a cloudless day, the deep sky offers a background with good thermal contrast for the measurement of the spectrum of atmospheric water vapor. Figure 5 shows the calibrated spectrum of a deep sky measurement. For this test, nine cubes of  $320 \times 256$  pixels were co-added and the spectral resolution was set to  $0.25 \text{ cm}^{-1}$ . Water vapor emission lines are seen in the  $1100$  to  $1250 \text{ cm}^{-1}$  region. Also, ozone emission is seen in the  $1000$  to  $1075 \text{ cm}^{-1}$  region.

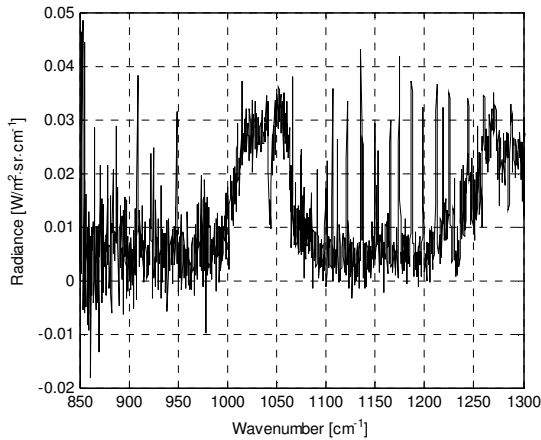


Figure 5: Deep sky calibrated measurement of the center pixel with  $0.25 \text{ cm}^{-1}$  spectral resolution

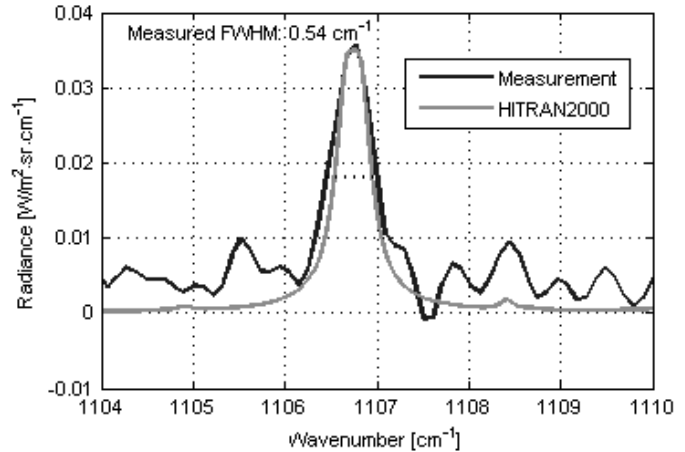


Figure 6: Zoom on the water vapor emission line at  $1106.745 \text{ cm}^{-1}$

MOLSPECT with HITRAN2000 database was used to compare the experimental results with theory. The parameters indicated in Table 2 were used to generate the data. A simplified model of the atmosphere is assumed, using a single layer of gas. It was determined that an appropriate spectral line to determine the spectral resolution of the FIRST-LW is situated at  $1106.745 \text{ cm}^{-1}$ .

TABLE 2 : Assumed conditions to generate the atmospheric spectrum with HITRAN2000

Atmospheric condition	Value	Unit
Relative humidity	50	%
Water vapor partial pressure	8.77	mm Hg
Depth of gas sample	1	km
Gas temperature	20	°C
Atmospheric pressure	1	atm

On Figure 6, the measured spectrum is superimposed on the normalized HITRAN2000 spectral signature near the above-mentioned line. The FWHM of the measured emission line is  $0.54 \text{ cm}^{-1}$ . However, the width of the atmospheric water vapor line strongly depends on the atmospheric conditions (vertical temperature and humidity profiles). The

expected width can lie anywhere between 0.3 and 0.7  $\text{cm}^{-1}$ , so by getting a measurement of 0.54, we can conclude that the FIRST resolution is better than 0.5  $\text{cm}^{-1}$ . By design, the expected spectral resolution is 0.25  $\text{cm}^{-1}$ , and another experiment setup is needed to measure it.

## 5. NESR

The sensitivity of infrared hyperspectral sensors based on Fourier transform spectrometers is generally specified in Noise Equivalent Spectral Radiance (NESR). Our NESR model was used to predict the performance of the FIRST hyperspectral sensor. Measurements performed in a field campaign allowed to validate the model experimentally.

### 5.1. NESR Theory

The NESR can be calculated theoretically with the well known relation (2).

$$NESR = NEP / (0.5 \cdot \tau \cdot ME \cdot \Theta \cdot \Delta\sigma \cdot t^{1/2}) \quad (2)$$

where  $NEP$  is the Noise Equivalent Power; [ $\text{W}/\text{Hz}^{1/2}$ ]  
 $\tau$  is the sensor transmittance; [-]  
 $ME$  is the modulation efficiency; [-]  
 $\Theta$  is a single pixel throughput; [ $\text{m}^2 \text{sr}$ ]  
 $\Delta\sigma$  is the spectral bin spacing; [ $\text{cm}^{-1}$ ] and  
 $t$  is the measurement time. [s]

The main complexity in accurately predicting a sensor NESR is to properly evaluate the NEP associated with all the noise contributors, notably the scene and instrument shot noise, the dark current noise, the readout noise, the electronics noise and the quantization noise. In the case of the FIRST sensor, the use of a focal plane array with integrating wells and readout electronics requires special attention for the associated NEP calculations. In particular, the signal filtering from the boxcar integrating function needs to be taken into consideration.

Table 3 summarizes the sensor operating parameters for which the NESR presented in this paper is evaluated.

The sensor transmittance and modulation efficiency used in the model were measured experimentally. The throughput for a single pixel of the sensor is calculated from its aperture and field-of-view.

TABLE 3. First sensor operating parameters

Parameter	Units	Value
Spatial resolution	pixels	320 x 128
	mrاد	112 x 45
Spectral resolution given by FWHM of the ILS (instrument lineshape)	$\text{cm}^{-1}$	4
Measurement time for a single sweep (one symmetrical double-sided interferogram)	s	3.13
Sensor transmittance (at 10 $\mu\text{m}$ )	%	83
Sensor modulation efficiency (spectral average)	%	75
Single pixel throughput	$\text{m}^2 \text{sr}$	$1.15 \times 10^{-10}$
Scene temperature	K	288
Sensor temperature	K	305
Detector integration time	$\mu\text{s}$	300
Detector sampling time	ms	2.64
Radiometric calibration blackbody measurements (at 288 K and 298 K)	-	10

The model allows predicting the spectral dependency of the sensor NESR. It is calculated for each noise contribution independently. The total NESR is estimated by calculating the RSS (Root Sum Square) of all the noise contributions, thus assuming that they are not correlated. The results are shown in Figure 7.

### 5.2. Experimental Results

The FIRST sensor was operated in a field-campaign in the United Kingdom in June 2005 (refer to section 6.2 for more details). Measurements were performed in the field with the same operating parameters as those presented in Table 3. These measurements allowed to measure the sensor NESR, and to compare the experimental results to the model results, as shown in Figure 8.

In order to evaluate the NESR from experimental data, a two-point radiometric calibration technique, described in detail in [2], is implemented. Two sets of blackbody measurements – one with a cold blackbody and one with a hot blackbody – are required. These measurements enable to calculate the sensor gain and offset which are used to perform the radiometric calibration (as explained in [1]).

Next, a sequence of scene measurements is acquired, with a blackbody positioned in the sensor field-of-view. This represents the ideal scene to measure the NESR, as the temporal variations of the scene radiance are negligible with a well controlled blackbody.

Thus, the NESR is evaluated spectrally by calculating the temporal standard deviation of the measured radiance for each measured spectral bin.

The NESR measurement was performed for each pixel in the 128x128 central zone of the detector. Next, the bad pixels were eliminated from the group, and the remaining 97% of the pixels were averaged to give the measured spectral NESR shown in Figure 8.

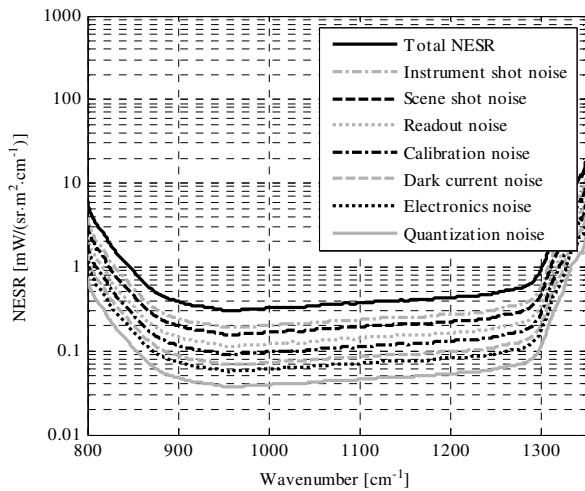


Figure 7: Predicted FIRST sensor spectral NESR.

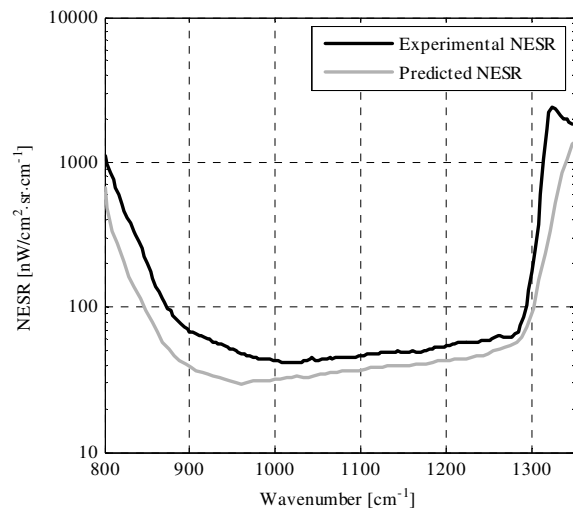


Figure 8: Measured and predicted FIRST sensor spectral NESR.

Note that the general NESR increase around  $850 \text{ cm}^{-1}$  is due to the detector cut-off, while the NESR increase above  $1280 \text{ cm}^{-1}$  is due to the optical cold filter in front of the focal plane array. The discrepancy observed between the predicted and experimental NESR between  $950$  and  $1250 \text{ cm}^{-1}$  is around 20%. Note that some parameters used in the model are known with an accuracy of  $\sim 20\%$ , and thus, the agreement obtained between the predicted and measured NESR is satisfactory.

## 6. Radiometric Accuracy and Stability

The radiometric calibration of FTIR instruments used for remote sensing was developed and refined in the late 1980s [1]. The result of this work yielded a simple and powerful calibration approach that corrects for instrument response, accurately removes the instrument self-emission and corrects for phase characteristics of the FTIR.

Radiometric calibration basically consists in characterizing the FTS response by a linear expression, i.e. by a gain (or slope) and an offset. The gain and offset are characterized as a function of the wavelength, and they are complex to represent the phase of the FTS as well. These gain and offset include the response of the interferometer, of the detector and of the associated electronics. Thus, the linearity of the detector and associated electronics is important. This concept

is explained in detail in a previous paper [2]. From the information obtained in the calibration process, one can study the absolute radiance accuracy and the radiometric accuracy.

The absolute radiance accuracy of a remote sensing instrument is one of its fundamental characteristics. Physical parameters derived from field spectra are directly affected by the ability of the sensor to produce measurements with good radiometric fidelity.

The stability of the radiance accuracy over time, often referred to as the radiometric stability, is equally important. It dictates the frequency at which the radiometric calibration process needs to be performed. In this paper, a large quantity of experimental calibration data acquired during two field campaigns in the summer of 2005 is used to analyze the radiometric stability of Telops' FIRST sensor. This study has the flavor of similar studies that were performed on other FTIR sensors, e.g. the study of the DRDC Valcartier CATSI radiometric stability presented in [3].

### 6.1. Radiometric Accuracy

The radiometric accuracy was measured by comparing the calibrated spectrum measurement of an external blackbody with its theoretical radiance. The comparison is made in brightness temperature units. The external blackbody temperature was set to 30°C.

Figure 9 shows the spectral radiometric accuracy in Kelvin. It is better than 0.5 K over the spectral range of the sensor.

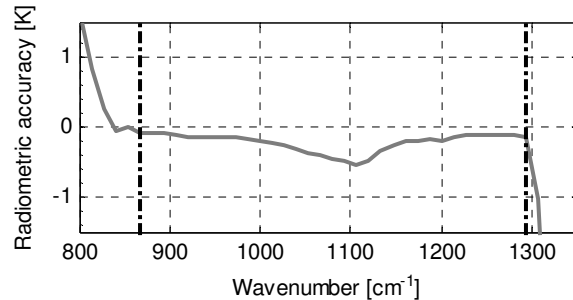


Figure 9: Spectral radiometric accuracy measurement

### 6.2. Experimental Data for Radiometric Stability Analysis

The FIRST sensor was used in two major field campaigns in the summer of 2005. First, it was used in a four-week campaign in England in June 2005. This trial was held at DSTL in Porton Down. Telops staff operated the FIRST sensor during this campaign aimed at testing standoff gas detection with remote sensors. The gas detection results are presented in section 7 and in more details in [7]. A photograph of the sensor at the Porton Down trial is shown in Figure 10.

Second, the FIRST sensor was used in a two-week field campaign in Utah in July 2005. This trial was held at Dugway Proving Grounds near Salt Lake City. Staff from the Johns Hopkins University Applied Physics Laboratory operated the loaned Telops' FIRST sensor in this campaign. They shared their calibration data with Telops for the purpose of this study.

The calibration data acquired during these two field campaigns was analyzed in order to study the FIRST radiometric stability. 120 radiometric calibrations were performed during the Porton Down trial, and 41 radiometric calibrations were performed during the Dugway campaign. Thus, the experimental data consists in a total of 161 radiometric calibrations acquired in two different continents over a 2-month time interval.



Figure 10: FIRST sensor at the DSTL campaign in Porton Down, UK

All the results presented in this paper are based on this data. Figure 11 shows the ambient temperature and the sensor temperature (measured on the modulator) over the entire time of the field campaigns. The ambient temperature varied between 15 and 33°C, and the sensor temperature varied between 18 and 42°C. Note that the zero time reference is 7 June 2005 at midnight.

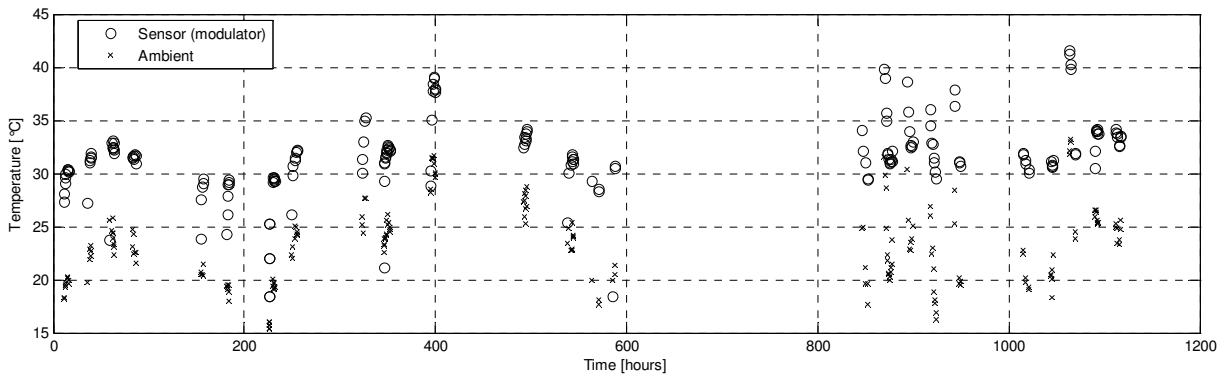


Figure 11: Ambient and sensor temperatures during the field campaigns. Seemingly vertical groups represent the usual daily temperature increase or nocturnal decrease.

The sensor was operated with fixed parameters during the two campaigns. The parameters are a centered spatial window of  $320 \times 128$  pixels, a spectral resolution of  $4 \text{ cm}^{-1}$ , a focus adjustment at infinity and blackbody temperatures adjusted to approximately 5 degrees Celsius below and above ambient temperature (for the cold and hot reference targets).

Note that during the two field campaigns, the FIRST sensor was used without taking advantage of its sensor temperature stabilization feature. This feature consists in heaters that are strategically positioned on the sensor key parts; i.e. the interferometer and the lens mechanical assemblies. These heaters can be used to maintain the instrument temperature stable regardless of the ambient temperature fluctuations. By disabling this feature, the data acquired allowed to evaluate the radiometric stability as a function of the instrument temperature fluctuations.

### 6.3. Experimental Radiometric Calibration Stability Analysis

Figure 12 shows the magnitude and phase of the gain averaged over all the good pixels, for all the 161 radiometric calibrations of the two field campaigns. The gain magnitude decrease in the  $850 \text{ cm}^{-1}$  region is caused by the detector cut-off, while the gain decrease around  $1300 \text{ cm}^{-1}$  is due to the presence of an optical cold filter in front of the detector. The spectral shape in this data shows that there is a significant advantage to characterize the gain as a function of the wavelength, as a lot of spectral variations are not considered if only a broadband calibration is performed. This illustrates an advantage that a spectral sensor has over a broadband sensor to achieve accurate radiometry.

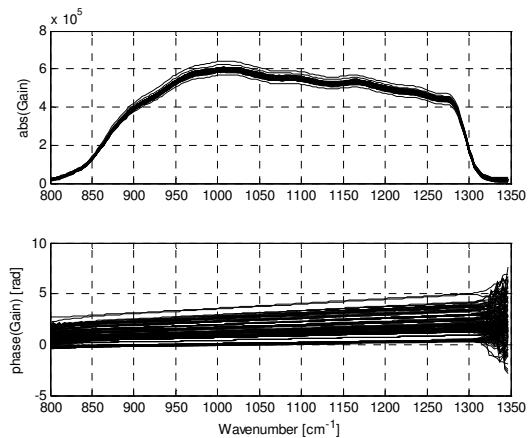


Figure 12: Measurements of the magnitude and phase of the gain, averaged for all pixels

The result from Figure 12 indicates that the spectral shape of the gain magnitude has not changed significantly during the entire time lapse. Given this observation, the analysis of the gain magnitude simply considers the fluctuations that are observed on the spectral average of the gain magnitude, between  $900$  and  $1250 \text{ cm}^{-1}$ .

Also, the results for all the good pixels are averaged together in order to reduce the noise level. “Bad” pixels - roughly 3% of the  $40,960$  pixels of the  $320 \times 128$  window that was used in the field campaigns - are excluded from this averaging.

Figure 13 shows the magnitude of the offset of all the calibration measurements, averaged for all the good pixels, in units of brightness temperature. The phase of the offset is also shown. The offset of all pixels is very similar to the radiance spectrum of a cold blackbody. This is because the sensor has a good transmittance, and thus a low radiometric offset. Furthermore, since the instrument is in a 2-port configuration, the contribution of the output port to the radiometric offset is very low, as the detector is cooled down to 68 K.

The offset is very low (~215 K), which indicates that the shot noise coming from the instrument radiance is minimized. This helps to reduce the noise level, since the FIRST is shot noise limited.

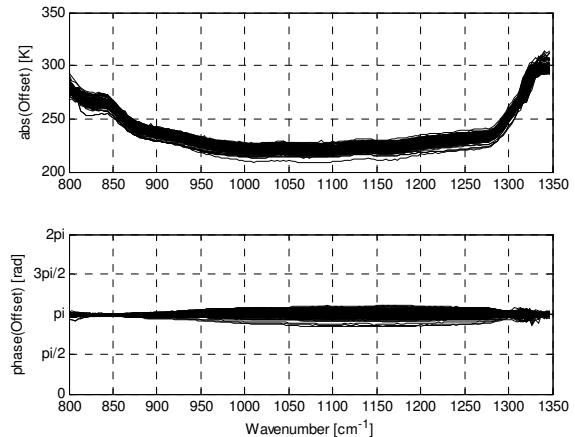


Figure 13: Magnitude of the offset in brightness temperature, averaged for all pixels

The detailed analysis of the radiometric stability was presented in [2]. The result indicates a total radiance accuracy of 1.8% ( $\sqrt{1.6\%^2 + 0.6\%^2 + 0.6\%^2}$ ). We emphasize that this level of accuracy is obtained with simple temperature compensation and without recalibrating the instrument by measuring calibration blackbodies. It is also implied that a phase correction is performed when the sensor is turned off and back on. The radiometric accuracy obtained right after a calibration is presented on Figure 9.

## 7. FIRST as a Standoff Chemical Detector

Several chemicals, including some mixtures, were released during the field test conducted in England in June 2005. The FIRST, combined with gas detection algorithms developed by Telops, was capable of detecting and identifying the various chemicals released [7]. Since the FIRST also gives temporal information, we are able to produce videos of chemicals clouds as they disseminate. The measurement rate of the FIRST depends on the image size and spectral resolution. When used at  $4 \text{ cm}^{-1}$  of spectral resolution with an image size of  $320 \times 128$ , the measurement rate is approximately 1 datacube every 4 seconds. This is enough to see continuous gas cloud displacement. Figure 14 presents typical examples of gas detection measurements. They present the broadband IR image in background with an overlay of the chemicals detected and identified. The overlay has a variable transparency. Where the scores of 2 different criteria are above the thresholds, the transparency is displayed and it is proportional to the score of a clutter-matched filter calculation. This gives an indication of the concentration of the chemical and this also displays clearly the cloud shape. Telops' web site ([www.telops.com](http://www.telops.com)) has video files from FIRST measurements that can be downloaded and played. They give a very good feeling of the powerful standoff chemical agent detection and identification capability of the FIRST.

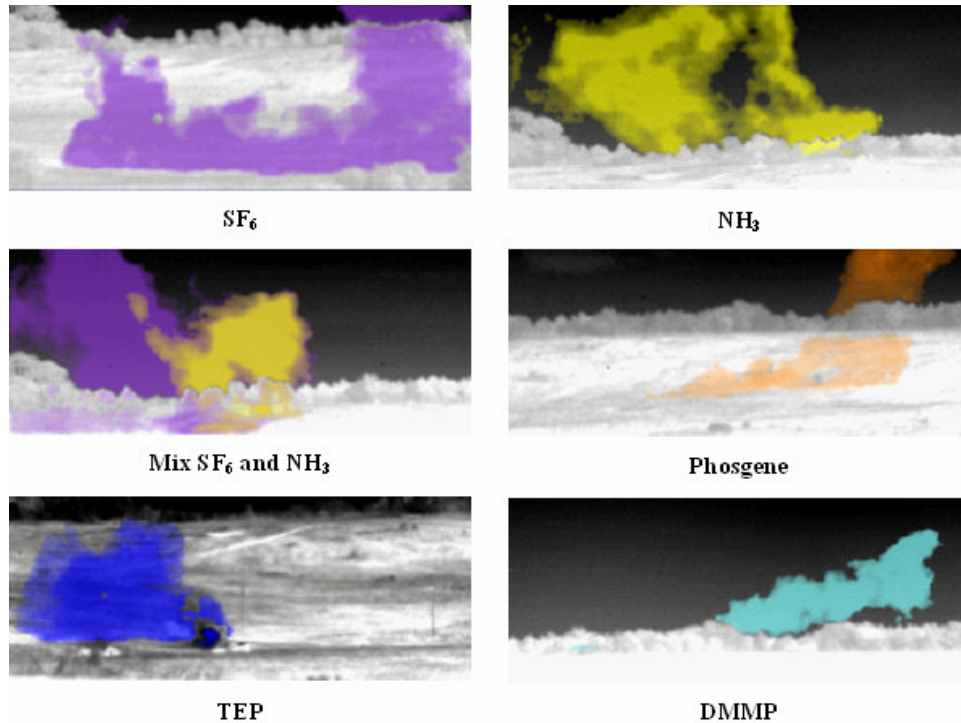


Figure 14. Typical results of chemical detection obtained with the FIRST

## 8. Conclusion

Telops has developed a powerful and versatile imaging spectrometer. The FIRST, operating in the LWIR band, is well suited for standoff chemical agent detection and can be used as a powerful hyperspectral imager for any scientific application. Excellent spectral resolution coupled to a high sensitivity are used to identify the chemical agents and discriminate interferences. The spatial and temporal resolutions allow the detailed tracking of gas cloud evolution that should provide invaluable information to the chemical cloud dispersion modeling community.

It was shown in this paper that over a period of 40 days, the radiance accuracy of the FIRST sensor remains better than 2%, with a single radiometric calibration. This assumes that the sensor temperature is stabilized, or that a linear correction based on the instrument temperature is applied on the gain phase and offset magnitude. This also implies that a phase correction is performed when the sensor is turned off and back on. This radiometric stability measured in the field underlines the quality of the FIRST sensor.

It was also shown in this paper that a simple spectral calibration of the FIRST sensor ensures a spectral accuracy of  $0.3 \text{ cm}^{-1}$  for each pixel, when using a  $0.5 \text{ cm}^{-1}$  spectral resolution. This assumes that a simple correction for the instrument lineshape is performed. The stability of the spectral calibration over time will be characterized in future tests.

## Acknowledgements

Telops would like to gratefully acknowledge the data contribution of the Johns Hopkins University Applied Physics Laboratory. Telops would also like to thank DSTL for the invitation to a field-campaign in June 2005, as well as the Department of National Defence of Canada for funding the production of the FIRST sensor and our participation to the field-campaign under a Defence Industrial Research (DIR) program.

## REFERENCES

- [1] H.E. Revercomb, H. Buijs, H.B. Howell, D.D. Laporte, W.L. Smith, and L.A. Sromovsky, *Radiometric calibration of IR Fourier transform spectrometers: Solution to a problem with the high-resolution interferometer sounder*; Applied Optics, vol. 27, issue 15, pp. 3210-3218, August 1988.
- [2] Vincent Farley, Martin Chamberland, Alexandre Vallières, André Villemaire and Jean-François Legault, *Radiometric Calibration Stability of the FIRST : a Longwave Infrared Hyperspectral Imaging Sensor*, Proc. SPIE Vol. 6206, Infrared Technology and Applications XXXII;
- [3] A. Villemaire, M. Chamberland, J. Giroux, R. L. Lachance, J.-M. Thériault, *Radiometric calibration of FT-IR remote sensing instrument*; Proc. SPIE Vol. 3082, pp. 83-91, Electro-Optical Technology for Remote Chemical Detection and Identification II; Mahmoud Fallahi, Ellen A. Howden; Eds., July 1997.
- [4] M. Chamberland et al., *Advancements in field-portable imaging radiometric spectrometer technology for chemical detection*, Proc. SPIE Vol. 5416, pp. 63-72, Chemical and Biological Sensing V; Patrick J. Gardner; Ed., August 2004.
- [5] V. Farley et al., *Development and testing of a hyper-spectral imaging instrument for field spectroscopy*, Proc. SPIE Vol. 5546, pp. 29-36, Imaging Spectrometry X; Sylvia S. Shen, Paul E. Lewis; Eds., October 2004.
- [6] M. Chamberland et al., *Development and testing of a hyper-spectral imaging instrument for standoff chemical detection*, Proc. SPIE Vol. 5584, pp. 135-143, Chemical and Biological Standoff Detection II; James O. Jensen, Jean-Marc Theriault; Eds., December 2004.
- [7] A. Vallières et al., *High-Performance Field-Portable Imaging Radiometric Spectrometer Technology For Chemical Agent Detection*, Proc. SPIE Vol. 5590, pp. 211-219, Optically Based Materials and Optically Based Biological and Chemical Sensing for Defence II; John C. Carrano, Arturas Zukauskas, Anthony W. Vere, James G. Grote, François Kajzar; Eds., October 2005.
- [8] C. A. Klein, R. P. Miller, and D. L. Stierwalt, *Surface and bulk absorption characteristics of chemically vapor-deposited zinc selenide in the infrared*, Applied Optics, vol. 33, issue 19, pp. 4304-4313, 1994.